# Fast electron injection and transport angles in high intensity laser-solid interactions

Contact:*paul.mckenna@strath.ac.uk

**M. Coury**, D. C. Carroll[1], X. H. Yuan[2], , R. J. Gray, M. N. Quinn, O. Tresca, D. A. MacLellan, H. Powell and P. McKenna*
*Department of physics, University of Strathclyde, SUPA, Glasgow G4 0NG, UK*

[1] *also with Central Laser Facility, STFC RAL, Oxfordshire OX11 0QX, UK*
[2] *Present Address: State Key Laboratory of Transient Optics and Photonics, Xiâan Institute of Optics and Precision Mechanics,Chinese Academy of Sciences, Xiâan 710119,China*

A.P.L. Robinson, C. M. Brenner[1], and D. Neely
*Central Laser Facility, STFC RAL, Oxfordshire OX11 0QX, UK*

M. Burza and C.-G. Wahlström
*Department of Physics, Lund University, P.O. Box 118, S-22100 Lund, Sweden*

Y. T. Li and X. X. Lin
*Beijing National Laboratory of Condensed Matter Physics Institute of Physics, CAS, Beijing 100190, China*

## INTRODUCTION

The generation and transport of laser-driven fast electrons in overdense plasmas is a crucial issue for the success of the fast ignition approach to inertial confinement fusion (ICF), the optimization of secondary radiation sources and the acceleration of ions by sheath fields. The injection of the fast electron beam and the role of self-generated resistive magnetic fields (B-fields) at the edges of the beam, pinching the beam, are particularly important to the fast ignition scheme. Whether the beam collimation occurs or not is highly dependent on the fast electron beam source divergence[1]. The criteria, in terms of fast electron beam properties, required to achieve ignition also depend on the electron beam divergence[2].

Experimental studies with metallic targets, using diagnostics based on measurements of transition radiation and X-ray emission, have shown that the beam divergence increases with the laser intensity, from $\sim 17°$ at $4 \times 10^{19}$ W/cm$^2$ to $\sim 27°$ at $5 \times 10^{20}$ W/cm$^2$ (for picosecond laser pulses)[5,6]. Recent hybrid-PIC simulations conducted by Honrubia and Meyer-ter-Vehn[2] concluded that in order to reproduce these measured fast electron beam divergence angles, a larger injection angle of $\sim 50°$ is required. The smaller beam transport angle arises due to magnetic collimation, which is strongest in the region of the electron source where the beam current density is highest[1,7]. The magnetic pinching has been invoked to explain recent experimental results[8–10]. The fact that the fast electron beam might be injected within a large angle motivates further theoretical and experimental investigations of fast electron injection and transport, so that the laser pulse parameters required to achieve fast ignition can be more accurately scaled. It has also led to theoretical and experimental studies producing collimated or focused fast electron beams[11–13].

In this report, we present a summary of results from a recent investigation of the injection and transport divergence angles of fast electron beams in solids irradiated by ultraintense, picosecond laser pulses. Coury *et al*[10] reports on a fuller presentation and discussion of these results.

## EXPERIMENTAL SETUP

The Vulcan Petawatt laser, providing p-polarized laser pulses with energies up to 400 J in a pulse duration of $\sim 0.8$ ps at a wavelength $\lambda$ of 1.054 $\mu$m, was focused onto layered metallic targets at an incident angle of 23°, using an f/3 off-axis parabolic mirror (OAP). The peak intensities, $I_L$, reach $\sim 4 \times 10^{20}$ W/cm$^2$ as the laser energy on target, $E_L$, is $\sim 30$ % of the total laser energy. The layered targets, referred to as Al-Cu-Al, are 5 mm $\times$ 5 mm foils of a 100 to 500 $\mu$m Al as a generation and propagation layer, a 5 $\mu$m Cu fluorescent layer and a 1 $\mu$m Al layer designed to prevent fluorescence from the fast electrons spreading laterally on the target rear surface[14].

Two-dimensional (2D) images of the Cu K$\alpha$ X-ray emission are recorded using a spherically bent Bragg crystal that images emission from the fluorescent layer onto a FujiFilm BAS image plate detector. The magnification is set to 10 and the crystal angle is set at 1.31° satisfying the Bragg condition in the second diffraction order for Cu K$\alpha$ at 8.048 keV.
The Proton beam spatial and energy distributions are recorded using radiochromic films (RCF). The RCF stack (HD 810) are positioned at 4 cm, viewing the target rear surface and covering an energy range from 1.2 MeV up to 40 MeV .
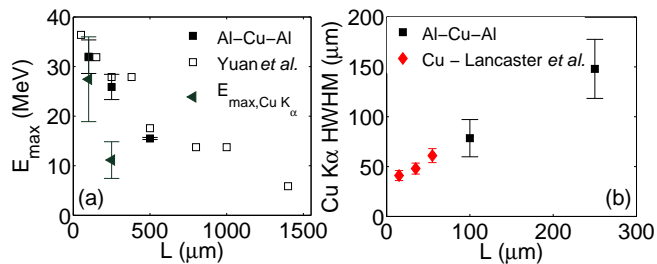
Figure 1: (a) Maximum proton energy, $E_{max}$, as a function of target thickness. Black squares are data obtained with Al-Cu-Al layered targets and the white squares are reproduced from Yuan *et al.*[9] (same laser parameters). Green triangles are theoretical estimates of $E_{max}$, calculated with estimates of the rear-surface fast electron density inferred from the Cu K$\alpha$ measurements shown in (b); (b) Measured lateral extent of Cu K$\alpha$ emission, half-width-at-half-maximum (HWHM), as a function of target thickness (front Al transport layer), $L$. Black symbols are data from the present experiment, from the Al-Cu-Al targets. Red symbols are measurements made with similar laser pulse parameters on Cu targets, reproduced from Lancaster *et al.*[5].

## EXPERIMENTAL RESULTS

Figure 1 presents the experimental results. Figure 1(a) shows the lateral extent (half width at half maximum, HWHM) of the Cu K$\alpha$ signal. No clear K$\alpha$ signal was recorded for targets thicker than 250 $\mu$m. The K$\alpha$ distribution (HWHM) as a function of target thickness follows the trend reported by Lancaster *et al*[5], of K$\alpha$ fluorescence measurements from thinner Cu foils, made with the same laser and very similar laser pulse parameters, as shown in Figure 1(a). A beam transport half-angle of between 10° and 38° is inferred from a linear fit applied to the new data points, and the corresponding limits are 17° and 31° if all data points shown are included. The best fit is for half-angle equal to $\sim$ 24°.

Figure 1(b) shows the measured maximum proton energy, $E_{max}$, as a function of $L$. Good agreement is also found with the results published in Yuan *et al*[9], obtained in similar experimental conditions and Al targets.
The simultaneous measurement of K$\alpha$ fluorescence, providing the lateral extent of the electron beam close to the target rear surface, and the measurements of the TNSA-generated proton beam, resulting from the fast electron-induced sheath field at the rear surface, enables a comparison between both diagnostics of the fast electron beam diameter. To do this, the electron beam radius inferred from the K$\alpha$ measurements determine the fast electron density at the target rear surface. The resulting beam density is then used in analytical model calculations of proton acceleration.
A detailed description of the analytical model and the numerical simulation runs can be found in Coury *et al.*[10].

## PLASMA EXPANSION MODEL RESULTS

The analytical model predicts the maximum proton energy using the Mora 1D isothermal plasma expansion formula[15]. The beam temperature $kT_e$ equal to 6 MeV is calculated from the ponderomotive scaling[16], for a peak laser intensity equal to $4 \times 10^{20}$ W/cm$^2$ and wavelength equal to 1.054 $\mu$m. The beam rear density is estimated as $N_e/(\pi r_{rear}^2 c\tau_L))$, where $r_{rear}$ is the fast electron beam radius at the target rear, $c$ is the speed of light and the number of fast electrons, $N_e$, is determined as $\eta_{L-e}E_L/kT_e$, where $\eta_{L-e}$ is the laser-to-fast electron energy conversion efficiency, $k$ is the Boltzmann constant and $T_e$ is the fast electron beam temperature.

Example model outputs are shown in Figure 1(a). The maximum proton energies were calculated for $L$=100 $\mu$m and 250 $\mu$m with $\eta_{L-e}$=0.5. The absolute values are not important as these depend on $\eta_{L-e}$. Within the expected range of $\eta_{L-e}$, a good match to the measured $E_{max}$ is found for the thin target. However, the relative decrease in the calculated $E_{max}$ as function of target thickness is much larger than the experimental one. The disparity between the two trends may be due to the assumptions in the simplified 1D model. To investigate the fast electron injection and transport physics in more detail, simulations of fast electrons transport in solids have been performed, as described below.

## 3D HYBRID-PIC SIMULATIONS

Using the 3D hybrid-PIC code ZEPHYROS[12,20], a series of simulations were performed as a function of target thickness in the range $L$=75-250 $\mu$m. The average injection angles and energy conversion efficiencies were varied in order to investigate the effects of these parameters on fast electron transport. Simulations were also performed with the self-generated resistive B-field suppressed. The resulting fast electron beam parameters at the target rear surface were extracted to calculate the expected maximum proton energy for comparison to experiment.

The simulations were performed using a 500 $\mu$m $\times$ 500 $\mu$m $\times$ $L$ $\mu$m box with grid size equal to 2 $\mu$m $\times$ 2 $\mu$m $\times$ 2 $\mu$m. The runs were performed for $L$=75, 100, 150, 200 and 250 $\mu$m. The lower limit of $L$, equal to 75 $\mu$m, was chosen to minimize the fast electrons refluxing in thinner targets on both front and rear boundaries, which affects the electron density evolution. The upper $L$ limit is set by computational limitations. The fast electron source input parameters were chosen to match the experimental parameters. The two variable source parameters are $\eta_{L-e}$ (and hence the number of fast electrons, $N_e$) and the angle of injection. The electron energy distribution, shown in Figure 2(a), is given by $N_e(E_e) = N_e exp(-E_e/kT_e)$. Electrons of energy $E_e$ were uniformly injected within a cone
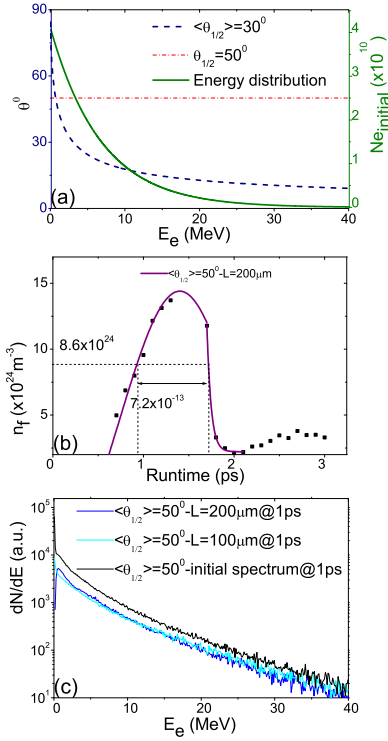
Figure 2: (a) Fast electron beam injection half-angle as a function of electron energy. The dashed blue curve is the distribution function derived by Moore *et al.*[21], with $\alpha = 1$ giving a mean half-angle $< \theta_{1/2} > \sim 30°$ in the example shown. The dashed red line corresponds to electrons injected uniformly within a cone with half-angle equal to $50°$. The solid green curve is the initial fast electron energy spectrum for a beam temperature of 6 MeV; (b) Temporal evolution of the maximum fast electron density at the target rear side, extracted from a hybrid-PIC simulation in 200 $\mu$-thick target, with $< \theta_{1/2} > = 50°$; (c) Fast electron energy spectra extracted from the hybrid simulations at the front side ('initial spectrum') and rear side of 100 $\mu$m and 200 $\mu$m-thick targets.
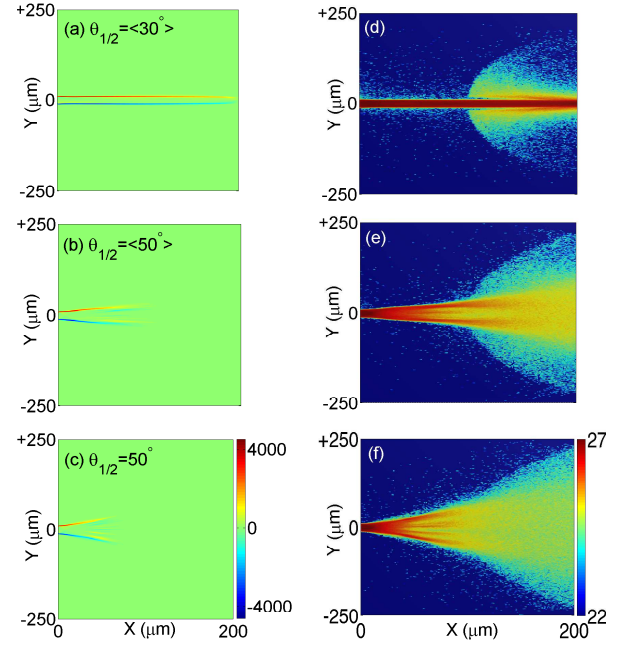


Figure 3: (a-c) False-color 2D profiles of the z-component of the self-generated resistive B-field (in units of Tesla); (d-f) Corresponding false-color 2D profiles of the fast electron beam density ($\log_{10}$ ($m^{-3}$)). The results are for a 200 $\mu$m-thick Al target and 1 ps run-time, at given $< \theta_{1/2} >$ specified in (a-c). The fast electrons are injected at position (0,0,0) and propagate in the direction of the x-axis. The grid size for these example simulations was equal to 1 $\mu$m $\times$ 1 $\mu$m $\times$ 1 $\mu$m to enable small-scale features to be resolved.

with half-angle $\theta_{1/2}$, examples of angular distribution functions are shown in Figure 2(a). Mainly, the distribution function derived by Moore *et al.*[21] was used: $\theta_{1/2} = \tan^{-1}[\alpha \times \sqrt{2/(\gamma - 1)}]$, where $\gamma$ is the electron Lorentz factor and $\alpha$ is a parameter which defines the average injection angle $< \theta_{1/2} >$ ($\alpha$=1 corresponds to the angle at which electrons are ejected from the laser focal spot by the ponderomotive force).

The peak fast electron density, $n_f$, and the ion acceleration time, $t_{acc}$, both input parameters in the plasma expansion model[15], were extracted from the simulations. A time-averaged value for $n_f$ was determined over the width of the main peak in the density-time profile, hereafter referred to as $n_{f-peak}$, and the FWHM duration of the peak was used for $t_{acc}$, as shown for the example in Figure 2(b).

Finally, Figure 2(c) shows examples of the initial electron energy spectrum and the spectrum at the rear side of a $L$=100 $\mu$m and $L$=200 $\mu$m target. A fit of the form

$\exp(-E_e/kT_e)$ gives no measurable change in $kT_e$, and this parameter was fixed at 6 MeV.

A series of simulation runs were performed, by (1) variation of $< \theta_{1/2} >$ at a fixed $\eta_{L-e}$ or (2) variation of $\eta_{L-e}$ at a fixed $< \theta_{1/2} >$, to investigate the sensitivity of fast electron beam transport to the injection angle at the source. $< \theta_{1/2} >$ was varied from $30°$ to $70°$ and the resulting $n_{f-peak}$ and $t_{acc}$ variations with $L$ determined. Generally, for a given $L$, $n_{f-peak}$ decreases rapidly with increasing divergence, which is expected due to increased lateral spreading of the electrons within the target. For $< \theta_{1/2} >=40°$ and above, $n_{f-peak}$ decreases with increasing $L$, also due to increased lateral spreading in the thicker targets. However, as the injection angle is decreased the resistive azimuthal B-field produced at the edge of the beam, shown in Figure 3, acts over a longer beam propagation length, and in the case of $< \theta_{1/2} >=30°$ acts to pinch or collimate the electrons over the full simulation box.

Furthermore, the effect of the self-generated B-field is investigated by performing simulations with the B-field suppressed. Even in the case of the relatively large $< \theta_{1/2} > \sim 50°$, the B-field strongly affects the electron density distribution within the beam and in particular the maximum electron density at a given depth in the target. The $n_{f-peak}$ values are significantly lower when the B-field is suppressed, irrespective of target thickness.

By comparing the fast electron density distributions and the B-field distributions (Figure 3) for $< \theta_{1/2} >$=50° and $\theta_{1/2}$=50°, it can be noticed that for a given average angle of electron injection, the form of the angle-energy distribution does have some effect on the B-field generation and therefore the fast electron transport. However, these parameters are observed to depend much more sensitively on the magnitude of the average injection angle.

Note that for low values of $< \theta_{1/2} >$ for which a high $n_{f-peak}$ is achieved (due to magnetic pinching), the peak temporal width is small, and a lower peak density is associated with a 'wider' peak and hence larger $t_{acc}$. These correlations suggest that the resistive B-field not only affects the fast electron density distribution within the beam, but also the temporal evolution of the resulting sheath field. For most of the simulation runs $t_{acc}$ is between 0.5 and 1.0 ps. Further investigation of the sheath field dynamics will be reported in a future publication.

Finally, the lateral extent of the fast electron beam determined from the simulations are close to the measured extent of the Cu $K\alpha$ emission. However, the beam size for the different injection angles simulated remains within the error bars of the $K\alpha$ extent, therefore no conclusions can be drawn from the Cu $K\alpha$ fluorescence measurements.

**Calculated maximum proton energies**

As discussed above, the values of $n_{f-peak}$ and $t_{acc}$ extracted from the simulation results are used as input parameters to the Mora plasma expansion model[15]. The model being 1D, requires that the fast electron density profile should be uniform in the plane normal to the proton motion. Although, the density distribution deduced from simulations is non-uniform, the variation of the density in the region of the peak is small over a radius of the order of the Debye length, so that the electron density profile can be considered to be locally uniform in the region of interest.

Examples of calculated $E_{max}$ trend with $L$ are presented in Figure 4, where the aim is to obtain the closest match to the experimental data. Figure 4(a) shows model results for which $\eta_{L-e}$ is equal to 0.2 and $< \theta_{1/2} >$ is varied. Due to the pinching effect of the B-field, the predicted proton maximum energies for the smaller injection angles are much higher than the experimental $E_{max}$. This suggests that the fast electrons should be injected into a cone with a large half-angle in order to reduce the B-field strength, and thus the beam density at the simulation box rear boundary. Figure 4(b) presents the case where the resistive B-field is suppressed. In this case, a close $E_{max}$ trend to experiment is obtained for a smaller $< \theta_{1/2} >$=30°, but the percentage decrease in $E_{max}$ with increasing $L$ is much larger than the experimental measurement. In Figure 4(c), both $< \theta_{1/2} >$ and $\eta_{L-e}$ are varied. In general, $< \theta_{1/2} >$ must be large to ensure that realistic values of $E_{max}$ are obtained for small $L$ and that
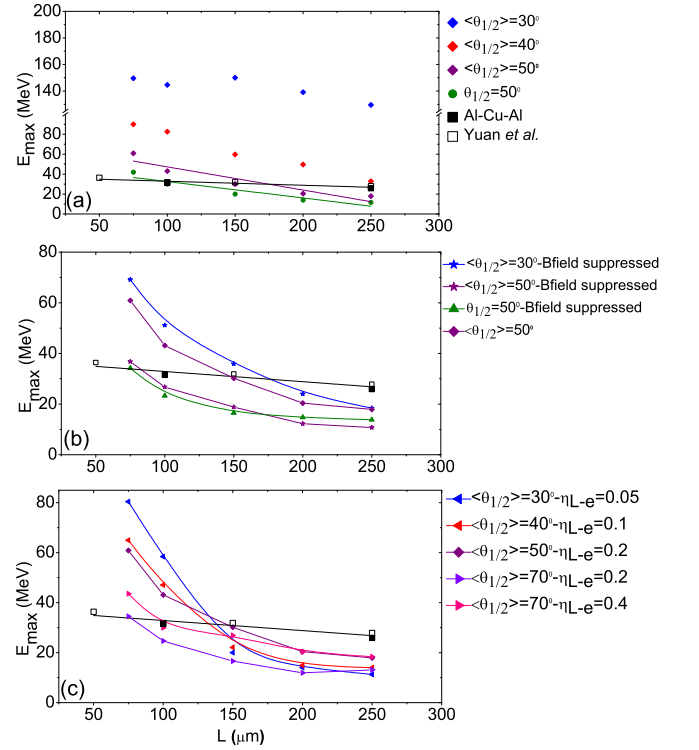


Figure 4: Maximum proton energy as a function of target thickness, $L$. As in Figure 1(b), black squares are data from the present experiment (Al-Cu-Al) and white squares are the measurements from Yuan et al.[9]. Coloured symbols are plasma expansion model calculations of $E_{max}$ using electron densities and ion acceleration times deduced from the hybrid simulation results of electron transport: (a) for fixed $\eta_{L-e}$=0.2 and given injection half-angles, $< \theta_{1/2} >$; (b) illustrating the effect of B-field suppression (for fixed $\eta_{L-e}$=0.2 and given $< \theta_{1/2} >$); and, (c) for given $\eta_{L-e}$ and $< \theta_{1/2} >$.

$\eta_{L-e}$ is relatively large to produce large $E_{max}$ in thick targets. The closest fit for the range of parameters investigated is found for $< \theta_{1/2} >$=70° and $\eta_{L-e}$=0.4.

The resulting fits are not ideal, nor unique solutions, but based on the large number of simulations conducted over a wide range of $< \theta_{1/2} >$ and $\eta_{L-e}$ (and the different angle-energy injection distributions), the average fast electron injection angle has to be large to reproduce the measured $E_{max} - L$ distribution.

**CONCLUSION**

The injection and transport divergence properties of a high current beam of hot electrons in metallic targets irradiated by high power, picosecond laser pulses is investigated using simultaneous measurements of $K\alpha$ fluorescence and proton acceleration, and 3-D hybrid-PIC simulations. The $K\alpha$ fluorescence measurements indicate that the effective transport half-angle is between 10° and 38° (17° and 31° if previous measurements with the same laser are included) as defined by the degree of uncer-

tainty in the measurements (best fit $\sim 24°$), and this is supported by the simulation results. The simulations further reveal that beam transport is strongly affected by self-generated magnetic fields, which in turn are sensitive to the average injection angle of the electrons at the front side of the target.

A comparison of the measured maximum proton energies with plasma expansion calculations performed using results from the electron transport simulations, indicates that the injected beam divergence at the source is larger (between $\sim 50 - 70°$) than inferred from previous studies performed with similar laser and target parameters. Our results support the predictions by Honrubia and Meyer-ter-Vehn[2] and the study by Solodov et al.[8] that suggest that the fast electron initial divergence angles are actually quite large. Strategies for controlling fast electron beam collimation are therefore likely to be important for Fast Ignition.

## ACKNOWLEDGMENTS

[1] A. R. Bell and R. J. Kingham, Phys. Rev. Lett. **91**, 035003 (2003).
[2] J. J. Honrubia and J. Meyer ter Vehn, Plasma Phys. and Control. Fusion **51**, 014008 (2009).
[3] L. Gremillet et al., Phys. Rev. Lett. **83**, 5015 - 5018 (1999).
[4] M. Borghesi et al., Phys. Rev. Lett. **83**, 4309 - 4312 (1999).
[5] K. L. Lancaster et al., Phys. Rev. Lett. **98**, 125002 (2007).
[6] J. S. Green et al., Phys. Rev. Lett. **100**, 015003 (2008).
[7] J. R. Davies et al., Phys. Rev. E **59**, (1999).
[8] A A Solodov et al., Journal of Physics: Conference Series **244**, 022063 (2010).
[9] X H Yuan et al., New J. Phys. **12**, 063018 (2010).
[10] M. Coury et al., Phys. Plasmas **20**, 043104 (2013).
[11] A. P. L. Robinson and M. Sherlock, Phys. Plasmas **14**, 083105 (2007).
[12] S. Kar et al., Phys. Rev. Lett. **102**, 055001 (2009).
[13] A.P.L.Robinson et al., Phys. Rev. Lett. **108**, 125004 (2012).
[14] P. McKenna et al., Phys. Rev. Lett. **98**, 145001 (2007).
[15] P. Mora, Phys. Rev. Lett. **90**, 185002 (2003).
[16] S. C. Wilks and W. L. Kruer, IEEE J. Quantum Electron **33**, 1954 - 1968 (1997).
[17] J.R. Davies, Plasma Phys. Control. Fusion **51**, 014006 (2009).
[18] P. McKenna et al., Laser Part. Beams **26**, 591 - 596 (2008).
[19] R. H. H. Scott et al., Phys. Plasmas **19**, 053104 (2012).
[20] P. McKenna et al., Phys. Rev. Lett. **106**, 185004 (2011).
[21] C. I. Moore, J. P. Knauer, and D. D. Meyerhofer, Phys. Rev. Lett. **74**, 2439 - 2442 (1995).

# Laser specular reflectivity as a function of target Z

**Contact** *bruno.gonzalez-izquierdo@strath.ac.uk*

**B. Gonzalez-Izquierdo and P. McKenna**

*SUPA, Department of Physics, University of Strathclyde, Glasgow, G4 0NG, UK*

**A. Green and M. Borghesi**

*Centre for Plasma Physics, School of Mathematics and Physics, The Queen's University of Belfast, Belfast BT7 1NN, UK*

**R. Deas, R. Moss and R. Giordmaina**

*Defense Science & Technology Laboratory, Fort Halstead, Sevenoaks, Kent, TN14 7BT, UK*

**D. Rusby*, H. Sandman, J. Green, C. Brenner, L. Wilson and D. Neely**

*Central Laser Facility, STFC Rutherford Appleton Laboratory, Didcot, Oxfordshire, OX11 0QX, UK*

**J. Wood and Z. Najmudin**

*Plasma Physics Research Group, Imperial College London, London, SW7 2AZ, UK*

## Introduction

Much of the interesting physics in the interaction of a high power laser pulse with a solid occurs in the region of the critical density in the preformed plasma at the front, irradiated surface. It is at the relativistically-corrected critical density surface, beyond which the laser pulse cannot propagate, that the laser pulse is reflected [1] and at which energy is absorbed to the production of fast electrons and high order harmonics generation (via the relativistically oscillating mirror (ROM) [2] model).

In this report, we present preliminary experimental results from an investigation of changes to specular reflectivity of an ultra-intense laser pulse as a function of the target atomic number, $Z$. Measurements are made at both the fundamental and second harmonic wavelengths. Moreover, we report on the fraction of the laser pulse energy which is converted to the second harmonic at close to the critical density surface and measured in the specular reflection path. Finally, we present measurements of specular reflectivity and the generated fraction of second harmonic radiation as a function of the peak laser intensity, for an example target material, tantalum.

## Experimental Setup

The experiment was carried out using the Vulcan laser, which delivered pulses on the target with energy in the range between 40 J and 75 J, in a 0.6 to 0.8 ps (FWHM) duration pulse, at wavelength 1055.5 nm. The configuration was formed by an f/3 parabola which focused the laser pulses onto targets at $35^{o}$ angle of incidence, with respect to the target normal direction, to a focal spot of ~5 μm in diameter, reaching intensities ~$10^{20}$ Wcm$^{-2}$. The target materials used included low atomic numbers such as CH-plastic, aluminum (Al) and copper (Cu), to higher atomic numbers like silver (Ag) and tantalum (Ta).
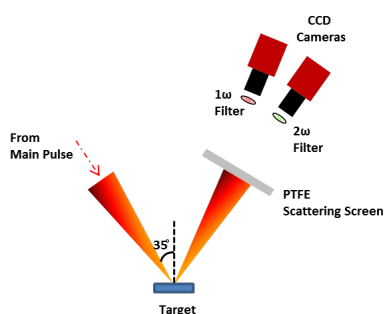


**Figure 1.** Experimental Set-up to measure the specular reflectivity at both the fundamental and second harmonic wavelengths.

A PTFE scattering screen was positioned in the path of the specularly reflected light and two CCD cameras were used to measure the spatial-intensity distribution of the specularly reflected beam. In front of each camera was placed a band-pass filter at 1ω or 2ω. Moreover, a neutral density filter was positioned facing the second harmonic filter to avoid saturation.

## Results and Discussion

Figures 2 and 3 show examples of the spatial-intensity distributions of the specularly reflected beam at 1ω and 2ω. These two figures show that at fundamental wavelength the reflected energy is quite regular, whereas at second harmonic a more irregular spatial distribution of the reflected energy is produced. The square shape of the reflected beam at 1ω is because of two large square mirrors positioned before the main parabola to steer the main beam.
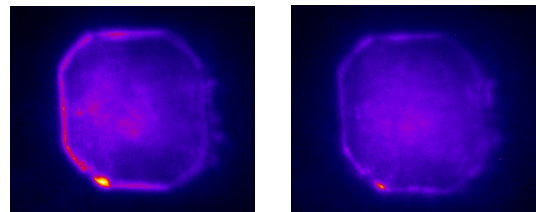


**Figure 2.** Example of the spatial-intensity distribution from specular reflected beam at 1ω for Cu (left) and Ta (right).
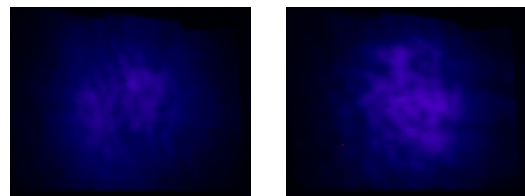


**Figure 3.** Example of the spatial-intensity distribution generated at 2ω in specular reflection for Cu (left) and Ta (right).

To calculate the reflected fraction of the laser energy from the input pulse, we integrated the spatial energy distribution on the PTFE screen as recorded by the two CCD cameras. The cameras show the intensity of each pixel of the image with an equivalent number of counts. To determine the energy calibration, i.e. the energy corresponding to the count number, we carried out a calibration shot for which a gold mirror was positioned in place of the target, to reflect a known laser pulse energy onto the PTFE screen.

The measured reflectivity of the 1ω laser light as a function conversion to 2ω light as a function of $Z$ is shown in figure 5. Figure 4 shows a slight variation of the reflectivity when we use target materials. There is a 25% difference between the material with the highest reflectivity (Cu) and the lowest (Ag), on average. Another interesting result from figure 4 is the overall very low reflectivity at 1ω, which is in the range of 2% to 2.5% for all materials (is not an unexpected value because it was not necessary to place any neutral density filter in front of the fundamental harmonic filter to prevent saturation). These results are distinctly different from measurements by Ping *et al* [3] and Streeter *et al* [4], which reported a specular reflectivity of around 30% at intensities of $\sim 10^{20}$ Wcm$^{-2}$, albeit using Ti:S laser pulses at 800 nm wavelength, with high contrast ($10^{-8}$-$10^{-10}$), and hundred and tens of femtoseconds pulse duration, respectively. However, Pirozhkov *et al* [5] shows that the specular reflectivity drops quickly to values lower than 10% for intensities $>10^{19}$ Wcm$^{-2}$ for relatively low contrast pulses (i.e. the ratio of the intensity in the main laser pulse to the intensity in the background amplified spontaneous emission, ASE).
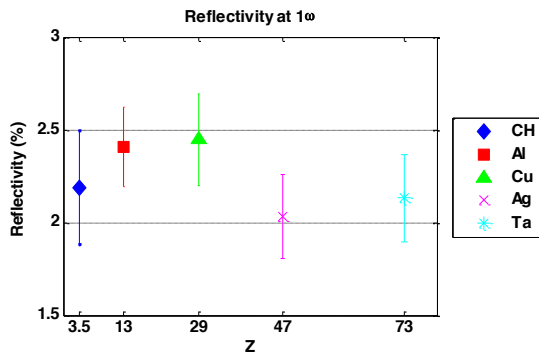


**Figure 4.** Specular reflectivity at 1ω as a function of target $Z$.

For the 2ω case, figure 5 shows a similar trend in terms of the scaling with target $Z$. However, this figure presents a relatively small conversion to the second harmonic, of around 0.7% of the incident laser energy (a factor of 3 times smaller than the specular reflectivity at 1ω).
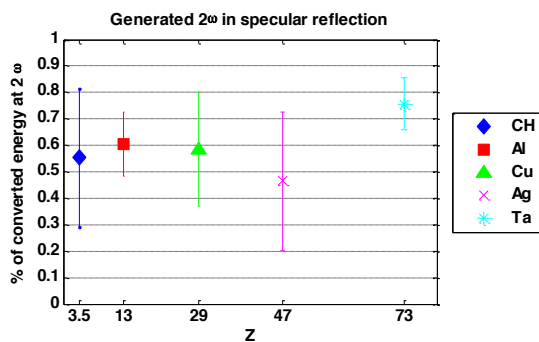


**Figure 5.** Generated 2ω in specular reflection as a function of target $Z$.

At fundamental wavelength, the highest reflectivity was obtained in Al and Cu targets, and the lowest in Ag and Ta, corresponding to the highest atomic number element used in the experiment. However, Ta was the material with the highest converted energy at second harmonic in specular reflection together with Al and Cu. Moreover, Ag presented the lowest energy conversion at 2ω in similar way to 1ω situation. The error bars are related to the standard deviation, and reflect shot-to-shot fluctuation in pulse energy and duration. The second harmonic generation is particularly sensitive to the properties of the drive laser pulse.

of target $Z$ is shown in figure 4 and the percentage laser energy

Taking Ta as example, we measured the specular reflectivity at 1ω and the generated energy fraction at 2ω as a function of the peak laser intensity on the target, as shown in figures 6 and 7, respectively. In these two figures each symbol corresponds to a single laser shot. The highest intensities were obtained placing the target in the best focus of the f/3 parabola, whereas to get the lowest intensities the target was positioned ~200 μm out of focus (i.e. defocused).

Figure 6 exhibits a smooth tendency of the specular reflectivity at fundamental harmonic, with a slight decrease with increasing laser intensity.
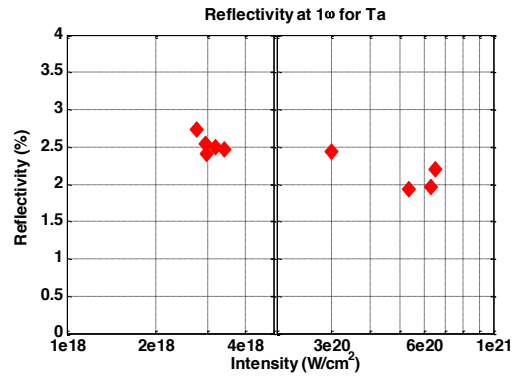


**Figure 6.** Specular reflectivity as a function of the peak laser intensity on Ta target at 1ω.

In turn, the generated fraction at 2ω presents a similar trend to the 1ω case being quite smooth at lower intensities. However, instead, it shows an increase of the converted energy in specular reflection when the laser intensity increase, as is exhibited in Figure 7.
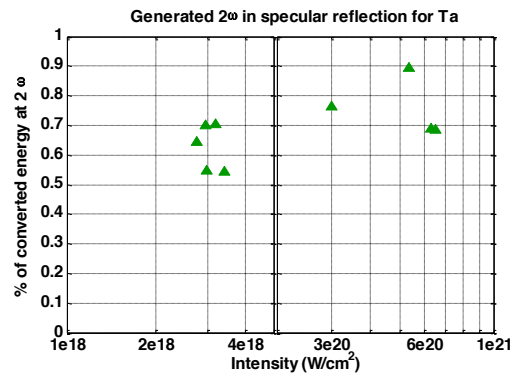


**Figure 7.** Generated 2ω in specular reflection as a function of the peak laser intensity on Ta target.

**Conclusion**

We have shown experimentally that the specular reflection of an ultra-intense laser beam on the front surface of a solid target as well as the conversion to second harmonic light in the specular reflection path exhibits a variation of ~25% when targets with different atomic number are used. Moreover, we have measured this as a function of peak laser intensity, in the case of Ta, and find little variation at low intensities, and a slight progressive decrease as the laser intensity is increased at fundamental frequency, and increasing the percentage of the converted energy at second harmonic when the laser intensity is increased as well. All results presented in this report, including the specular reflectivity at 1ω and the generated fraction at 2ω in reflection as a function of $Z$ and the scaling with peak laser intensity on the target (Ta case), are the subject of ongoing analysis and complementary simulations, aimed at obtaining a better understanding of the underlying physics.

**References**

1. S. Eliezer. The Interaction of High-Power Lasers with Plasmas. IOP Publishing Ltd, 2002.

2. C. Thaury and F. Quere. High-order harmonic and attosecond pulse generation on plasma mirrors: basic mechanisms. Journal of Physics B: Atomic, Molecular and Optical Physics, 43, 213001, 2010.

3. Y. Ping, et al. Absorption of Short Laser Pulses on Solid Targets in the Ultrarelativistic Regime. Physical Review Letters, 100, 085004, 2008.

4. M. J. V. Streeter, et al. Relativistic plasma surfaces as an efficient second harmonic generator. New Journal of Physics, 13(2):023041, 2011.

5. A. S. Pirozhkov, et al. Diagnostic of laser contrast using target reflectivity. Applied Physics Letters, 94(24):241102+, 2009.

# Ion beam characterisation from ultra-thin plastic foil targets under direct illumination with the Vulcan Petawatt

**Contact** *g.hicks11@imperial.ac.uk*

**G. S. Hicks, N. P. Dover, H. Nakamura, M. J. V. Streeter, Z. Najmudin**
*Blackett Laboratory, Imperial College London, London, SW7 2AZ, UK*

**H. Ahmed, S. Kar, M. Borghesi**
*Centre for Plasma Physics, Queen's University Belfast, Belfast, BT7 1NN, UK*

**D. A. MacLellan, P. McKenna**
*SUPA, Department of Physics, University of Stathclyde, Glasgow, G4 0NG, UK*

**C. Kreuzer, J. Schreiber**
*Department für Physik, Ludwig-Maximilians-Universität, München, Garching, 85748, Germany*

**J. Fernandez-Tobias, R. Heathcote, I. Musgrave, M. Notley, W. Shaihk, D. Neely**
*Central Laser Facility, STFC Rutherford Appleton Laboratory, Oxfordshire, OX11 0QX, UK*

## Introduction

Laser accelerated ion beams have received attention over the past few years, since they offer a compact, cost effective alternative to conventional accelerators for scientific and health care applications. [1,2]

With the development of CPA laser systems laser intensities have increased dramatically, and with new laser systems based on OPCPA systems laser intensities are set to increase further [3,4]. Therefore it is important to investigate mechanisms that have favourable ion energy scaling with laser intensity.

The majority of experimental research so far has focused on sheath acceleration (SA), where ion energies scale $\sim I^{0.5}$ [5]. The hole boring (HB) acceleration mechanism, that instead uses radiation pressure to drive the front surface of a laser irradiated target, is attractive since it has a more favourable energy scaling than sheath acceleration of $\sim I^1$ [6]. But it requires higher laser intensities and preferably lower density targets. For very thin targets, the whole target can experience this radiation pressure driven acceleration, leading to the light sail (LS) phase which potentially has an even better intensity scaling of $I^2$ [7]. Recent studies, though, have indicated that the ultra thin targets required for LS acceleration are often prone to instabilities [8]. Sheath acceleration gives thermal ion spectra, whereas HB and LS acceleration can give monoenergetic peaks.

An interesting regime between the sheath acceleration expected for thick targets and the radiation pressure dominated mechanisms expected for thin targets, is the relativistic transparency (RT) regime [9–11]. RT is similar to SA in that thermal ion spectra are produced, but the electron heating in the two regimes is very different. In SA, laser energy is only absorbed by electrons within a skin-depth of the front surface, whereas in RT the laser absorption quickly evolves into volumetric heating of the entire target volume beneath the laser focal spot. For thin enough targets, the target becomes relativistically transparent and the laser passes through the plasma. This mechanism leads to improved beam energies and conversion efficiencies over sheath acceleration.

All laser systems are subject to some sort of prepulse, in which laser light of a lesser intensity propagates along the beam path up to nanoseconds before the main pulse. A prepulse can destroy thin targets before the main pulse arrives, which has a detrimental effect on the ion acceleration.

Due to an improved OPCPA front end, (intensity) contrast ratios of $>10^{10}$ at 1 ns are now possible on the Vulcan Petawatt laser. This means that it is of interest to directly illuminate ultrathin targets without the use of plasma mirrors. This not only greatly simplified the experimental arrangement but also increased the energy available on target [12].

In this report we present data showing high-energy proton production from ultrathin formvar foils with thicknesses down to 25nm irradiated with Vulcan Petawatt without the use of plasma mirrors.

## Experimental arrangement

The experiment was carried out using the VULCAN laser in Target Area Petawatt. A laser pulse of energy 340 ($\pm$40) J (on-target) and duration 1.0 ($\pm$0.2) ps was focused into a focal spot containing 33% of the on-target energy into full-width half-maximum of 3.3 μm as measured with the CW alignment beam onto CH targets of thicknesses from 25 nm up to 3 μm at normal incidence with nominal intensity $\sim 1.7 \times 10^{21}$ Wcm$^{-2}$

The ion beam generated by the laser plasma interaction was diagnosed using radiochromic film (RCF) stacks [13]. RCF stacks were used to measure the dose deposited by the proton beam at discrete energy level and also to give the spatial intensity distribution of the proton beams for different energy levels. The RCF used was GafChromic HD810.
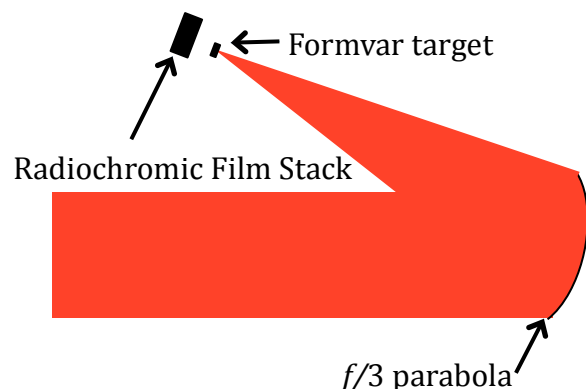


Figure 1 The experimental set up, showing the *f*/3 focusing parabola, target position and radiochromic film stack position.

## Results and Discussion

Proton beams were observed originating for targets with a range of thickness from 25–3000 nm. Maximum proton energies exceeding 50 MeV were regularly observed. Figure 2 shows spatial proton beam profiles from targets of thicknesses between 25 nm and 3 μm for the slice from the stack that corresponds to 14.7 MeV. For the thinner foils it is clear there is high

frequency spatial modulation of the beam. This due to modulations in the target surface, which focus the incoming laser beam. This leads to variation of the laser intensity across the target surface, which, due to the intensity dependence of the radiation pressure, reinforces the modulation. At certain points the laser breaks through the target leaving higher density regions of protons around the break through points. The whole foil, with this imprinted variation expands and is thus accelerated to moderately high energy, and so can be detected on the RCF stack. In this way, the higher dose filaments on the RCF indicate the structure of the foil at the time of this burn-through. This modulation of the proton beam profiles and its anti-correlation with the laser beam transmission has been reported before by C. Palmer et. al [8]
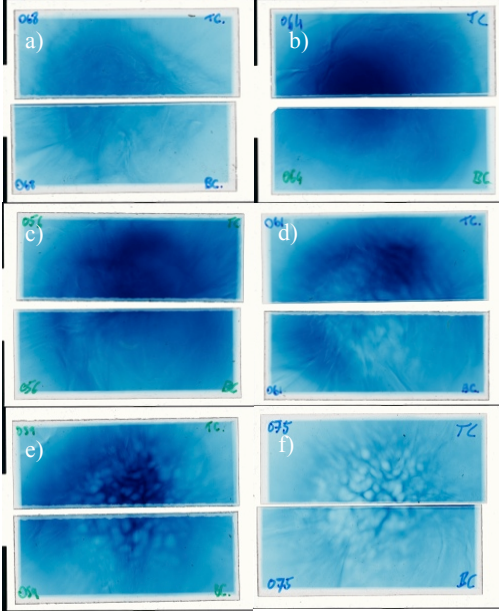


Figure 2 Radiochromic film showing the proton beam at at 14.7 MeV from 6 different shots from shots on formvar (CH) foils of thicknesses a) 3 μm b) 500 nm c) 250 nm d) 100 nm e) 50 nm and f) 25 nm. The stack had a maximum observation angle of 1.1 srad.

Figure 3 shows that there is an optimum thickness of target for achieving high maximum proton energies. For thinner targets modulation of the proton beam occurs, as shown in figure 2-e and 2-f (and somewhat in 2-d). However proton energies begin to fall again for thicker targets. Figure 3 suggests the optimum foil thickness is around 250 nm.
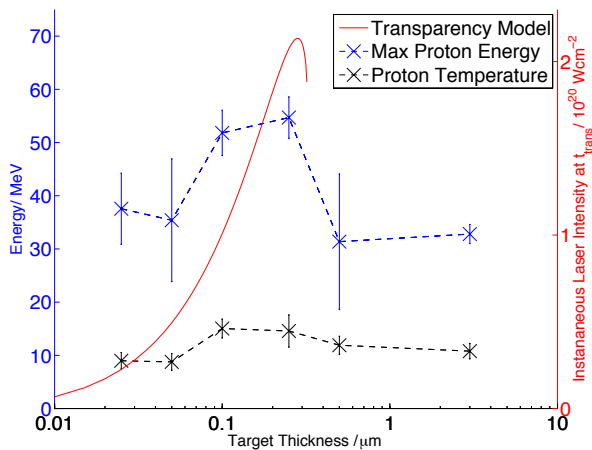


Figure 3: left axis; Maximum (blue) and mean (black) measured peak proton energies as a function of target thickness. Each data point is an average value for up to 4 shots at a particular target thickness. The error bars for a) and b) are calculated from the individual shot error, number of data points and spread of points. Red right axis: instantaneous laser

intensity at the time when the target becomes relativistically transparent as a function of target thickness. The laser intensity was decreased to 12% its experimental value to fit to the data. Targets thinner than 310 nm become relativistically transparent.

Figure 4 shows proton beam temperature as a function of foil thickness. Beam temperatures were calculated from an exponential fit to the data of the form $e^{\frac{-E_p}{T_p}}$. The advantage of plotting beam temperature instead of peak proton energy is that the beam temperature contains information from the entire spectrum or alternatively from every film in the stack, rather than only the last one. The coarse energy resolution of RCF as a spectrometer and the detection limit of the film limit the accuracy to which the maximum detected proton energy of the spectrum can be measured. The trend in the beam temperature is similar to the trend in the peak detected energy; as expected as high beam temperatures would be expected to correspond with high peak proton energies and conversely. The optimum thickness for both measures is between 100 and 250 nm.

We can assess if the dependence in thickness is given by the condition for light sail acceleration to occur. The requirement for this is that the time for the hole boring front to reach the rear surface of the target in a time $t_{hb}<t_l$, the laser pulse length [14].

The hole boring velocity can be expressed as,

$$v_{hb} = \sqrt{\frac{Z}{m_i c} \frac{1+R}{2} \frac{I}{n}}$$

Where $m_i$ is the ion mass, $c$ the speed of light, $R$, the reflectivity of the target, $I$, the laser intensity and $n$ the plasma electron density. For a $2.6\times10^{21}$ Wcm$^{-3}$ laser pulse the hole boring velocity, $v_{hb} = 1.1\times10^7$ ms$^{-1}$ for protons, assuming total reflectivity. At this velocity, the hole boring front would travel 11 μm in a laser pulse of length $t_l = 1$ ps. This $v_{hb}$ corresponds to a proton energy of ~660 keV, a factor of 80 smaller than the peak proton energy observed. For every target thickness used in this study $t_{hb} < t_l$, therefore the light sail mechanism was accessible for all target thicknesses and this does not explain the peak proton energy dependence on target thickness.

A model has been proposed by Henig et. al. [11], which can be used to predict the optimum target thickness for relativistic transparency due to target expansion for any given laser parameters. They demonstrate a direct connection between the instantaneous laser intensity at the time when the target becomes relativistically transparent and the resulting maximum ion energies.

But rather than taking a fixed fast electron temperature that drives the expansion, we make the assumption that the target is thin enough so that all the electrons are heated to the same temperature given by the ponderomotive potential,

$$T_e(t) = \frac{2}{3}(\gamma(t) - 1)m_e c^2$$

where $\gamma(t)$ is the the target Lorentz factor. The target expands at the ion sound speed,

$$c_s = \sqrt{\frac{Z_i T_e(t)}{m_i}}$$

where $Z_i$ is the nuclear charge, which in the case of a carbon dominated foil is $Z = 6$. There is no adiabatic index because the electron are assumed to be isothermal. The target thickness is assumed to vary with time as;

$$d(t) = d_0 + \int_{-\infty}^{+\infty} c_s(t)dt$$

where $d_0$ is the initial target thickness. Therefore the electron density will vary as

$$n_e(t) = n_0 \frac{d_0}{d(t)}$$

where $n_0$ is the initial target density. When the target density has reduced to below the relativistic critical density ($n_e < \gamma n_{cr}$) the target becomes relativistically transparent.

It has been suggested [11] that for optimal ion acceleration, the target should become transparent close to the peak of the laser pulse. Figure 3 shows the instantaneous laser intensity at the time when the target becomes relativistically transparent as a function of target thickness. The model used an intensity distribution, *I(t)*, based upon measurements provided by Vulcan laser staff, although the intensity was reduced to 12 % to fit with the data. The optimum thickness for the nominal intensity was 2 μm, whilst with this arbitrary reduction in intensity, the maximum thickness for transparency could be reduced to 312 nm.

This then is well correlated with the highest experimental peak proton energy, which was observed for a target of thickness 250 nm. Targets of 650 nm and thicker never become relativistically transparent in this model, explaining why the 3μm target had lower proton energies, and why the maximum proton energy observed for the 500 nm is already falling from the maximum.

During the experiment four shots were taken on 25 nm targets, for two of them the central beam was modulated and for two it was not. The non-filamented proton beams had a higher energy then the filamented proton beams; it appears that the break-up of the foil indicated by these modulated beams is detrimental to creating high-energy proton beams, since in this case it leads to burn-through of the foil at earlier times. The modulation reduces the beam temperature, with the temperature of the filamented beams being 9.5±0.6 MeV, whilst it was 14±4 MeV for the non-filamented beams.
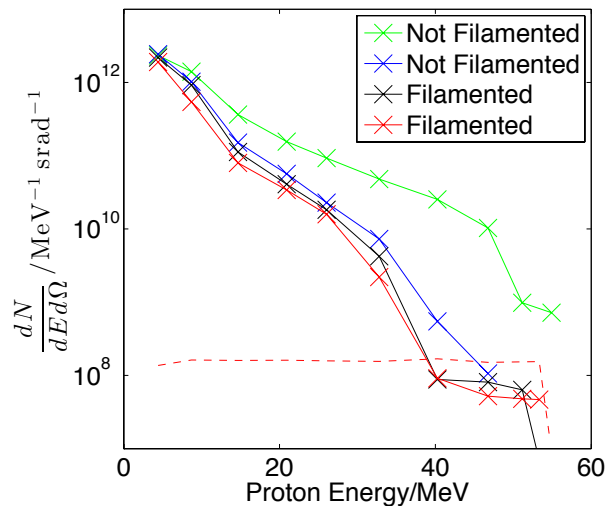


Figure 4 Proton spectra from modulated and non-modulated beams on 25 nm targets. The beam modulations can be seen to reduce the peak proton energy and proton temperature.

## Conclusions

We fielded radiochromic film stacks on an experiment in Target Area Petawatt on the Vulcan laser. Proton energies over 50 MeV were observed for targets of 250 nm down to 25 nm. Optimal foil thicknesses of 100 to 250 nm were observed although 54.9 MeV protons were observed from a 25nm thick target.

An analytical model for predicted optimum thicknesses for proton acceleration from relativistically transparent targets was used. The observed optimum of 250 nm agrees with the model for an intensity 12% of that measured.

It was observed that for very thin targets the modulation of the proton beam indicates unstable acceleration of the foil which leads to reduced peak proton energy and beam temperature.

## References

[1]     T. Tajima and J. M. Dawson, Physical Review Letters **43**, 267 (1979).

[2]     M. Murakami et al, AIP Conference Proceedings **1024**, 275 (2008).

[3]     D. Strickland and G. Mourou, Optics Communications **56**, 219 (1985).

[4]     C. Hernandez-Gomez et al, Journal of Physics: Conference Series **244**, 032006 (2010).

[5]     H. Daido, M. Nishiuchi, and A. S. Pirozhkov, Reports on Progress in Physics **75**, 056401 (2012).

[6]     T. Esirkepov et al, Physical Review Letters **92**, 2 (2004).

[7]     A. P. L. Robinson et al, New Journal of Physics **10**, 013021 (2008).

[8]     C. Palmer et al, Physical Review Letters **108**, 1 (2012).

[9]     L. Yin et al, Physics of Plasmas **14**, 056706 (2007).

[10]    L. Yin et al, Physics of Plasmas **18**, 063103 (2011).

[11]    A. Henig et al, Physical Review Letters **103**, 1 (2009).

[12]    T. Winstone et al, CLF Annual Report (2012).

[13]    D. Kirby et al, Laser and Particle Beams **29**, 231 (2011).

[14]    S. Kar et al, Physical Review Letters **109**, 185006 (2012).

# Probing the solid-liquid transition of carbon at ~150 GPa pressure using spectrally resolved X-ray scattering

**Contact**  *d.kraus@gsi.de*

**D. Kraus, J. Helfrich, A. Ortner, M. Roth**
*Technische Universität Darmstadt*
*Schlossgartenstr. 9, 64289 Darmstadt, Germany*

**N. Hartley, G. Gregori**
*University of Oxford*
*Parks Road, Oxford, OX1 3PU, UK*

**B. Kettle, D. Riley**
*Queen's University of Belfast*
*University Road, Belfast, BT7 1NN, UK*

**D. C. Carroll, M. M. Notley, C. Spindloe**
*Central Laser Facility*
*Rutherford Appleton Laboratory, Didcot, OX11 0WX, UK*

## Introduction

The understanding of carbon at extreme conditions is highly relevant to various fields of science [1-3]. These especially include planetary sciences and many laboratory applications where solid state carbon samples are heated very rapidly to a dense plasma state. Liquid carbon under more than 100 GPa pressure is predicted to exist inside Uranus and Neptune, because methane, which is highly abundant on the surface, is believed to pressure-dissociate in the interior. Carbon at comparable pressures and temperatures is also abundant in white dwarfs. Moreover, the recent discovery of extra-solar planets, which may consist of up to 50% of carbon, further raises the importance of carbon for this field. One possible application of carbon at these extreme conditions is the controlled realization of inertial confinement fusion in the laboratory. As carbon may be used as ablator material, an improved knowledge of the equation of state would enhance the accuracy of the simulations modelling the processes which are supposed to lead to ignition in the fusion capsule. Hereby, the microscopic structure is of special importance as this property defines the ratio between thermal and potential energy induced in the compression phase and, thus, has a high influence on the final temperatures. In this report, we present successful measurements of the microscopic structure of carbon close to the melting line, using spectrally resolved X-ray scattering from shock-compressed graphite samples.

## Experiment

The Experiment was performed at VULCAN, Target Area West, a schematic of the setup is shown in Fig. 1. Four of the frequency doubled Main-6 long pulse lasers with a total intensity of ~$10^{13}$ W/cm² were applied for shock compression of graphite samples. To achieve different final states behind the shock front, graphite types of different initial density were applied (flexible graphite 1.4 g/cm³, rigid graphite 1.84 g/cm³ and HOPG 2.26 g/cm³). For the characterization of the state behind the shock front, the shock transit times were recorded by an optical streak camera using the self-emission of the shock release (see Fig. 2). Comparison of the shock transition times with one-dimensional hydrodynamics simulations using the HELIOS code suite and the SESAME equation of state suggests that pressures of ~150 GPa were reached behind the shock front. Beam 8 was focused on a vanadium foil at ~$10^{17}$ W/cm² creating K-alpha X-rays at 4.95 keV with an energy conversion efficiency of ~5x$10^{-5}$. A typical source spectrum is shown in Fig. 3. For probing the homogeneous regions of the shock wave, the X-rays were collimated by a 500 µm pinhole which was included in a cone structure made of gold to ensure sufficient shielding. The scattered radiation at the scattering angles 28°, 50°, 105° and 125° was collected by spectrometers

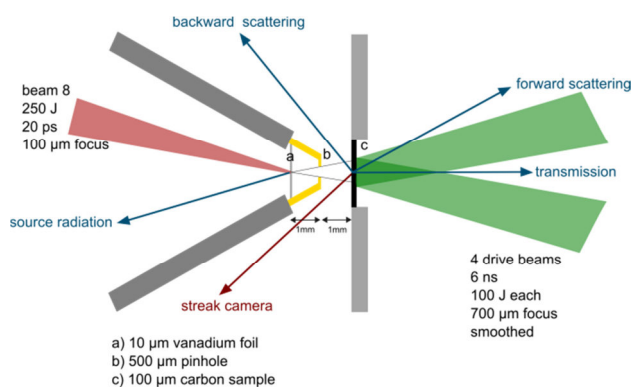using curved HOPG crystals in von-Hamos geometry. All X-ray spectrometers used image plates as detector.



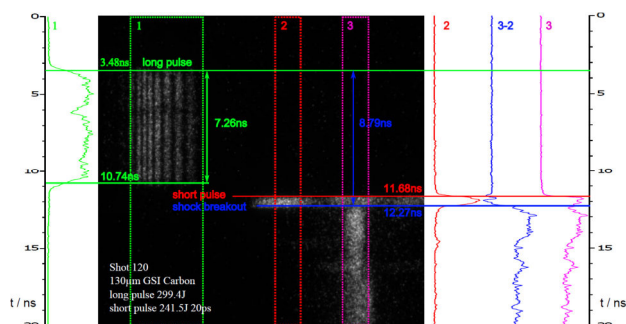*Figure 1. Sketch of the experimental setup.*



*Figure 2. Pulse timing and measurement of the shock release at the target rear side using an optical streak camera.*
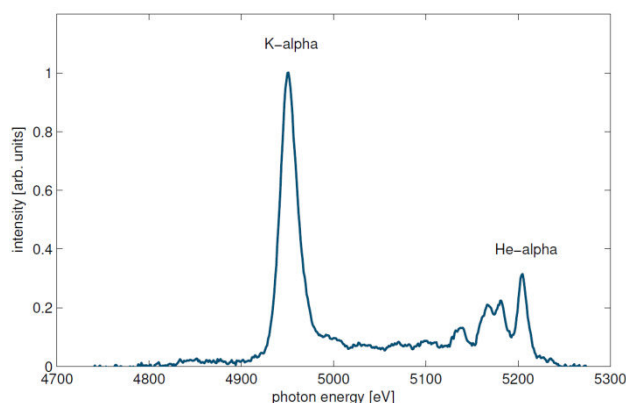


*Figure 3. Typical source radiation spectrum.*

## X-ray scattering from crystalline and liquid carbon

The scattered radiation power per solid angle is given by [4]

$$\frac{dP}{d\Omega} = I_0 \, r_0^2 \, \frac{1}{2} (1 + \cos^2 \theta) \, N \, S(k),$$

where $I_0$ is the incident X-ray intensity, $r_0$ the classical electron radius, $\theta$ the scattering angle and $N$ the number of sample atoms. $S(k)$ is the static electronic structure factor which contains all the structural information of the investigated sample material. By choosing a suitable photon energy and scattering angle, $S(k)$ can be decomposed to [5]

$$S(k) = |f(k)|^2 S_{ii}(k) + \sum_{n=1}^{Z_{wb}} [1 - f_n(k)^2].$$

The first term of this equation corresponds to elastic scattering from tightly bound electrons: $f(k)$ is the atomic form factor, $S_{ii}(k)$ the structure factor of the atoms or ions. The second term describes the inelastic scattering from $Z_{wb}$ weakly bound electrons with the corresponding single electron form factors $f_n(k)$. As the form factors are known, being able to separate between the two features in an experiment gives the possibility to directly obtain the atomic correlations via $S_{ii}(k)$ [6].

## Results

A sample scattering spectrum obtained by the HOPG spectrometer at 125° scattering angle is shown in Fig. 4. This spectrum is an average of three shots with similar conditions where flexible graphite was compressed. Here, the different scattering features can clearly be identified. The ratio of elastic and inelastic scattering directly gives the atomic structure $S_{ii}(k)$ using the X-ray source spectrum, which is measured in the experiment, and an inelastic bound-free Compton profile for input. This leaves $S_{ii}(k)$ as the only free parameter which is fitted to $S_{ii}(k) = 1.01 \pm 0.14$ in this case.
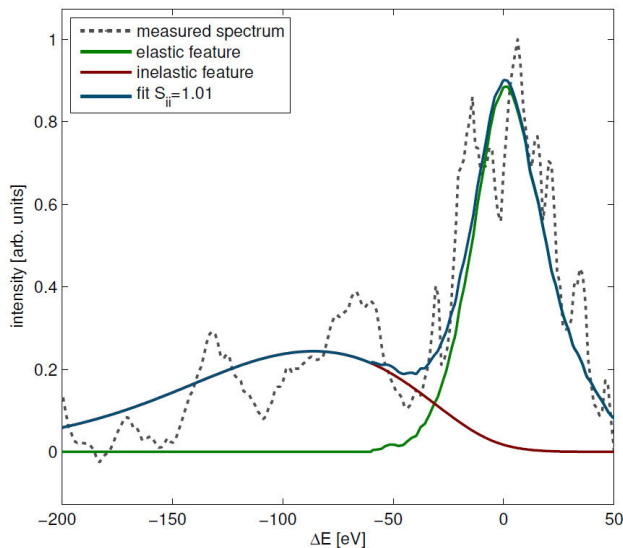


*Figure 4. X-ray scattering spectrum from which the structure factor is deduced by determining the ratio of elastic and inelastic scattering.*

Using this method, the structure change induced by the shock wave can be determined [7]. At 125° scattering angle, a value of $S_{ii}(k) \geq 0.4$ is consistent with a fluid phase according to ab-initio simulations of phases which might be present behind the shock front (liquid carbon, hexagonal diamond or cubic diamond) [8]. For flexible and rigid graphite targets, we measure a strong increase of the elastic scattering at this angle compared to scattering from cold samples where no elastic scattering could be recorded at this angle ($S_{ii}(k) < 0.2$). Thus, it can be stated that flexible and rigid graphite targets were driven into the liquid phase behind the shock front. For HOPG instead, the elastic scattering remained below detection threshold, comparable to cold samples. Thus, the temperature behind the shock front was not high enough to reach the melting threshold and the shocked state is most probably solid diamond (either hexagonal or cubic). This is in good agreement with one-dimensional hydrodynamic simulations using the HELIOS code suite. Combining all results, states very close to the melting line were produced in the experiment, both on the solid and the liquid regime next to the phase transition. The structure values, which will be obtained by further analysis of this experiment, can directly be compared to theoretical calculations of the structure factor.

## Conclusions

As a summary, it can be concluded that the presented method is able to characterize phase transitions in such extreme conditions. Using different types of graphite targets, we were able to cross the melting line of carbon at a relatively constant pressure of ~150 GPa. This can be used to constrain models of the carbon phase diagram not only by the position of the melting line but also by resulting values of the structure factor for the liquid phase.

## Acknowledgements

## References

1. A. A. Correa et al., Physical Review B **78**, 024101 (2008).

2. J. H. Eggert et al., Nature Physics, **6**, 40–43 (2009).

3. M. D. Knudson et al., Science **322**, 1822 (2008).

4. S. H. Glenzer and R. Redmer, Rev. Mod. Phys. **81**, 1625 (2009).

5. A. Pelka et al., Physical Review Letters **105**, 265701 (2010)

6. E. Garcia-Saiz et al., Nature Physics **4**, 940 (2008).

7. D. Kraus et al., High Energy Density Physics **8,** 46-49 (2012).

8. D. Kraus et al., submitted to Physical Review Letters (2013).